Sentinel-1 InSAR over Germany: Large-Scale Interferometry, Atmospheric Effects, and Ground Deformation Mapping

Mahmud Haghshenas Haghighi and Mahdi Motagh

Summary

In this study, three highlights of Sentinel-1 (S-1) Interferometric Synthetic Aperture Radar (InSAR) over Germany are presented to evaluate the potential and opportunities provided by this European SAR mission. Firstly, large-scale interferometry across the country is presented and analyzed against atmospheric models from ERA-Interim and GNSS (Global Navigation Satellite System) to assess the perspective provided by S-1 for atmospheric modeling and large-scale displacement analysis. We then analyzed localized deformations related to anthropogenic activities at two different regions using S-1 InSAR time-series analysis. In the first case study, small-magnitude (mm/yr) displacement related to underground gas storage and landfill compaction in Berlin is investigated. Despite low rates of displacement, Persistent Scatterer InSAR (PSI) using an extensive collection of S-1 data reflects both the long-term trend and seasonal variations related to dynamics of gas storage in the reservoir. We estimate long-term surface uplift of up to 2 mm/yr between October 2014 and January 2017 and seasonal variations of up to 2 cm due to charge and discharge of the reservoir during summer and winter periods. An old demolishing landfill NW of Berlin was also found to be subsiding with rates as much as 8 mm/yr. The other case study is a brown coal mining area south of Leipzig. Time-series of S-1 data using the Small BAseline Subset (SBAS) approach provides new insights into mining-induced deformations in this region. Our results show rapid subsidence of up to 4 cm/yr between October 2014 and April 2017 in two active open-pit mining areas in the region.

Zusammenfassung

In dieser Studie werden Anwendungsbeispiele von InSAR (Interferometric Synthetic Aperture Radar) in Deutschland vorgestellt, um Möglichkeiten und Chancen der europäischen SAR-Mission Sentinel-1 (S-1) zu bewerten. Zunächst werden großmaßstäbliche landesweite Interferometrie-Messungen beschrieben und atmosphärischen Modellen von ERA-Interim und GNSS (Global Navigation Satellite System) gegenübergestellt, um abzuschätzen, welche Möglichkeiten sich für atmosphärische Modelle und Displacement-Analysen durch S-1-Daten ergeben. Anschließend werden lokale, aus Sentinel-1-Zeitreihen (time-series analysis) erhaltene, anthropogen-bedingte Deformationen in zwei Regionen analysiert. Im ersten Regionalbeispiel (Berlin-Spandau) wurden kleinräumige Verschiebungen im mm-Bereich pro Jahr festgestellt (Hebungen im Untergrundgasspeicher bei Spandau und Absenkungen in einer alten Deponie, Lutoner Straße). Die Untersuchungen erfolgten mit der Persistent Scatterer InSAR-Methode (PSI). Nutzt man die zeitlich höher aufgelösten S-1-Zeitreihen, können sowohl Langzeittrends als auch saisonale Veränderungen bestimmt werden. Es wurden langfristige Hebungen (2 mm pro Jahr zwischen Oktober 2014 bis Januar 2017) sowie saisonale Veränderungen von bis zu 2 cm festgestellt (Gaseinspeicherung und -entnahme in Sommer- und Winterperioden). Die erwähnte ältere Mülldeponie im Berliner Nordwesten zeigt Absenkungsraten von etwa 8 mm pro Jahr (fortschreitende Kompaktion der deponierten Massen). Im anderen Fallbeispiel (Braunkohlenrevier südlich von Leipzig) lassen sich zwischen Oktober 2014 und April 2017 in zwei aktiven Abbaugebieten mit dem Small BAseline Subset (SBAS)-Ansatz in den Sentinel-1-Zeitreihen schnelle Absenkungen von bis zu 4 cm pro Jahr erkennen.

Keywords: Sentinel-1, Large-scale InSAR, Deformation, Atmosphere

1 Introduction

Since 1991, when the ERS-1 satellite was launched and then followed by ERS-2 and Envisat, European Space Agency (ESA) has been providing repeated SAR data for over two decades. Although ERS and Envisat missions were originally designed to be used mainly for oceanic applications, they also provided spectacular opportunities for scientists to use the interferometric capability of the system for a broad range of geophysical (Hole et al. 2007, Kumar et al. 2008, Motagh et al. 2008a, Pritchard and Fielding 2008, Samsonov et al. 2014) and environmental (Castel et al. 2000, Santoro et al. 2007, Lu and Kwoun 2008, Xiuming et al. 2008, Millin-Chalabi et al. 2014) applications. Using SAR acquisitions, repeated approximately from the same point in space at different times, InSAR provides the capability to derive the path-length differences in the scale of the carrier wavelength and below due to changes in topography (Massonnet and Feigl 1998, Bürgmann et al. 2000). However, conventional InSAR suffers from some severe limitations when unwanted signals in the interferograms, caused by various sources such as variations of scattering properties of earth's surface or atmospheric conditions through time, surpass the displacement signal (Hooper et al. 2012). Multi-temporal interferometric methods (MTI) including Persistent Scatter InSAR (PSI) (Ferretti et al. 2001, Hooper et al. 2004) and Small Baseline Subset (SBAS) (Berardino et al. 2002) present a specific class of processing that

exploits multiple SAR images acquired over an area in order to overcome these limitations and separate the displacement signal from other unwanted sources. The techniques are widely used by scientific communities to investigate surface deformations related to a broad range of geophysical (Hooper et al. 2007, Gourmelen et al. 2010, Haghshenas Haghighi and Motagh 2016, Motagh et al. 2017) and engineering (Fornaro et al. 2013, Milillo et al. 2016, Emadali et al. 2017) applications.

The idea of displacement monitoring in wide areas using standard InSAR or advanced InSAR time-series analysis has been an interesting topic in the last years (Motagh et al. 2008b, Motagh et al. 2010, Adam et al. 2013, Francesca et al. 2013, Raspini et al. 2015). A major limiting factor to this purpose was the non-availability of both spatially and temporally homogeneous SAR dataset in a nationwide or continental scale. The launch of Sentinel-1A in 2014, followed by Sentinel-1B in 2016, revolutionized the availability of SAR data by regular acquisition from every part of the world. S-1 obtains several frames of SAR data (250 × 250 km^2) along each observation track. Mosaicking the SAR frames provides then the possibility to monitor even larger areas along a specific track.

Sentinel-1 constellation is the follow-on to the former ESA SAR missions but is specifically designed to be suitable for InSAR applications and displacement monitoring. Therefore, its imaging parameters, revisit time, spatial resolution, scene coverage, and orbital status are optimized for InSAR applications (Salvi et al. 2012).

The operational lifetime of S-1 is expected to be 20 years. With both Sentinel-1A and Sentinel-1B in orbit this mission currently provides more than 10 TB of products every day. Based on its acquisition plans, SAR images from the same orbit are acquired every 6 days over Europe as well as some hotspots with very rapid changes like Greenland. In other parts of the world SAR data are acquired every 12 or 24 days.

In this study, three highlights of using S-1 InSAR over Germany are presented. In Germany, InSAR has been widely used in the past decades to address a variety of geological, geophysical, and engineering applications at local and/or regional scale, e. g. urban uplift due to geothermal energy production (Lubitz et al. 2013, Heimlich et al. 2015), monitoring tunneling processes (Liu et al. 2014), post-mining activities (Kircher et al. 2003, Wegmuller et al. 2004, Samsonov et al. 2013), deformations caused by subsurface mining (Wegmuller et al. 2000, Walter et al. 2009), pipeline monitoring (Werner et al. 2004), deformations induced by oil extraction (Fuhrmann et al. 2016), and water vapor mapping (Alshawaf et al. 2012).

Different SAR sensors, especially European ERS-1/2 and Envisat, and German TerraSAR-X satellites acquired SAR data over Germany in the last two decades. After the launch of Sentinel-1 constellation with its 6-day repeat interval, however, the availability of regular SAR data acquisition over the country has been dramatically

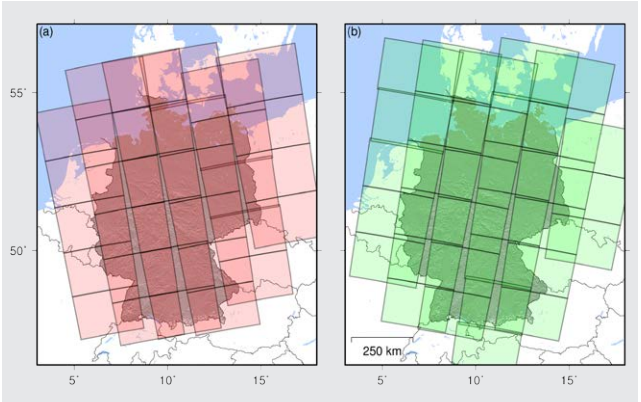

Fig. 1: Coverage of Sentinel-1 SAR images using the standard acquisition mode over Germany (highlighted by the shaded relief map) in (a) ascending and (b) descending tracks. Along each orbit, a few frames of SAR images are acquired which are represented by thick polygons.

increased. In total, as illustrated in Fig. 1, six ascending and six descending orbits of S-1 cover the whole country. Furthermore, there are some overlaps between data from neighboring orbits. Consequently, the coverage frequency of S-1 is as short as 1 to 2 days at any part of the country.

In the next sections of the paper, we first briefly describe InSAR processing of S-1 and InSAR time-series approaches. Then, we present an example of a large-scale interferogram with a short temporal baseline over Germany and evaluate it against tropospheric models provided by ERA-Interim and GNSS. In the following sections, two areas subject to localized displacements are investigated using S-1 InSAR time-series analysis.

2 Sentinel-1 InSAR processing

S-1 can collect SAR images in four different modes. StripMap (SM) and Extra Wide-swath (EW) are two modes that are implemented for consistency of the SAR data with those acquired by ERS and Envisat. Over the open ocean, the data is acquired in Wave Mode (WM). Nonetheless, Interferometric Wide-swath (IW) is the standard acquisition mode of S-1 over land, which is suitable for interferometric applications. In this mode, the data covers a swath of 250 km with a spatial resolution of ~5 × 20 m^2 in range and azimuth directions (Torres et al. 2012). To produce such a large coverage from a single acquisition in space, the SAR data in IW mode is acquired using the Terrain Observation with Progressive Scan (TOPS) operation (Zan and Guarnieri 2006).

A TOPS SAR image consists of three sub-swaths with ~2 km overlap, and each sub-swath is formed from several slightly overlapping subsets called bursts (see Fig. 2). The sensor does not record each sub-swath continuously, but records one burst of a specific sub-swath while the antenna is moving along its orbit. Then the antenna is steered so it can record one burst of another sub-swath.

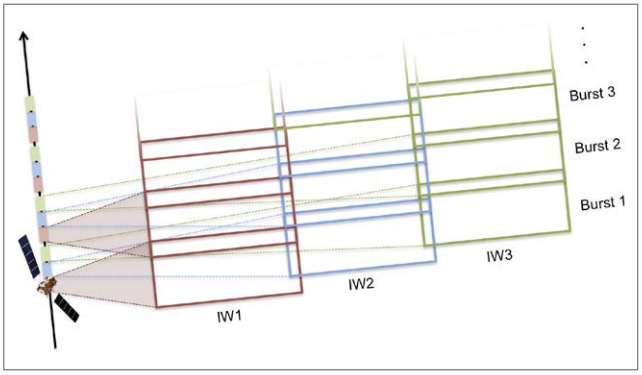

Fig. 2: Schematic illustration of Sentinel-1 TOPS mode imaging. The SAR image is acquired in three overlapping sub-swaths (IW1 to IW3) and each sub-swath consists of several overlapping bursts.

As a result of steering the antenna, a Doppler variation is present in the azimuth direction. To prevent this from causing any phase jump between subsequent bursts, the accuracy of coregistration between image pairs should be in the order of 1/1000 of azimuth resolution which is equivalent to a few centimeters on the ground (González et al. 2015).

Traditional coregistration approaches based on image matching cannot reach such a high level of accuracy needed for TOPS interferometry. However, together with orbital state vectors and terrain heights they can be used as a first order estimation of coregistration parameters (Yagüe-Martínez et al. 2016). Then, in an iterative approach, double difference interferograms in the overlapping areas between consecutive bursts are generated, and the coregistration parameters are refined by spectral diversity methods as described in Scheiber and Moreira (2000).

After precise coregistration of S-1 image pairs, they can be used, similar to other traditional SAR data in StripMap mode, to produce the interferometric phase, which can be expressed by the following equation:

$$\Delta\varphi = \varphi_{orb} + \varphi_{topo} + \varphi_{def} + \varphi_{atm} + \varphi_{noise}\,. \tag{1}$$

The interferometric phase in Eq. 1 is the sum of contributions from several factors including orbital status (φ_{orb}), topography (φ_{topo}), surface displacement (φ_{def}), atmospheric artifacts (φ_{atm}), and noise (φ_{noise}). When the interesting parameter is displacement, all other terms should be accounted for and removed from the interferometric phase.

The phase difference from orbital status is caused by the shift in the orbital path of two SAR acquisitions. Thanks to precise orbital state vector data of the Sentinel-1 satellites in the order of a few centimeters, this contribution can be compensated accurately (Yagüe-Martínez et al. 2016). The topographic phase contribution can be expressed as

$$\varphi_{topo} = -\frac{4\pi}{\lambda}\frac{B_{perp}h}{R\sin\theta}\,, \tag{2}$$

where λ, h, R, θ, and B_{perp}, are wavelength (5.6 cm for S-1), elevation of the target pixel above reference ellipsoid, distance between sensor and ground target, incidence angle, and perpendicular baseline of the interferogram, respectively. The topographic phase contribution is proportional to the perpendicular baseline of the interferogram. Therefore, smaller perpendicular baselines are preferred for deformation monitoring because they reduce the residual effect that might remain in interferograms by not completely removed topographic contributions, e. g. due to errors in the reference DEM (h). Because S-1 is designed to be suitable for deformation analysis, its orbit is maintained in a way that the perpendicular baseline is kept small in the order of 150 m (Yagüe-Martínez et al. 2016) and as a result, the sensitivity of S-1 interferograms to inaccuracies of DEMs is low.

The interferometric phase is also affected by differences in propagation delays through troposphere or ionosphere in the time of SAR image acquisitions. C-band SAR images in mid-latitudes are less susceptible to ionospheric effects (Hanssen 2001), and hence the major atmospheric contribution in S-1 interferograms in mid-latitudes comes from the troposphere. This effect is driven by the changes in refractivity of the troposphere at the time of two SAR acquisitions. The two-way slant range delay φ_{tropo} for a specific target at elevation h_1 in a SAR image can be expressed as:

$$\varphi_{tropo} = -\frac{4\pi}{\lambda}\frac{10^{-6}}{\cos\theta}\int_{h_1}^{h_2}\left(N_{hydro} + N_{wet}\right)dh\,, \tag{3}$$

where h_2 is the height of the effective tropospheric layer, and N_{hydro} and N_{wet} are refractivity corresponding to hydrostatic and wet delays. Two different categories of atmospheric corrections are typically applied on SAR interferograms. In the first category, the atmospheric effect is calculated and mitigated solely based on the phase information of the interferograms. For example, assuming the tropospheric effect behaves randomly in time, it is possible to average several interferograms from the same area to reduce the effect (Zebker et al. 1997). Furthermore, InSAR time-series approaches such as PSI or SBAS can also mitigate the tropospheric effects by filtering signals that are strongly correlated in space but not in time (Ferretti et al. 2001, Berardino et al. 2002).

The other category of atmospheric mitigation methods is based on external information, in which different sources, such as global atmospheric models, GNSS, or spectrometer data that provide information about the atmospheric condition at the time of SAR acquisition, are used for tropospheric correction of interferograms (Bekaert et al. 2015).

The other undesired contributions to the interferometric phase, produced by error sources such as phase decorrelation and soil moisture, are summed up in φ_{noise}, which are usually assumed to be negligible for displacement applications. After removing the unwanted phase

contributions from the interferogram, the remaining interferometric phase can be attributed to displacements by

$$\varphi_{def} = -\frac{4\pi}{\lambda}\Delta r, \quad (4)$$

where Δr is the displacement of the target pixel in the line-of-sight (LOS) direction that can be expressed in terms of a 3-dimensional displacement vector by

$$\Delta r = \left[-\cos\alpha\sin\theta \quad \sin\alpha\sin\theta \quad \cos\theta\right]\left[v_x \quad v_y \quad v_z\right]^T, \quad (5)$$

where α is the heading of the satellite and v_x, v_y and v_z are displacements in east-west, south-north and vertical directions, respectively. The imaging geometry of the SAR sensor (heading and incidence angle) defines its sensitivity to surface movement of the target pixel in three dimensions. Because SAR satellites, including S-1, move around the earth in polar orbits their heading angles are close either to 180 (for descending tracks) or 360 (for ascending tracks). Therefore, their measurements are more sensitive to displacements in vertical and east-west directions than to the north-south direction.

When S-1 interferograms are formed they can be adopted, similar to any other InSAR datasets, in time-series approaches. InSAR time-series approaches were initially developed to overcome the problem of phase decorrelation and atmospheric artifacts in conventional InSAR using long series of SAR data. In general, time-series methods produce a stack of interferograms, detect coherent pixels with high signal to noise ratio, estimate and reduce unwanted errors in the interferograms, and finally calculate the time-series and the average rate of displacement (Berardino et al. 2002, Ferretti et al. 2011, Hooper 2008).

Two different kinds of coherent pixels can be found in interferograms based on surface scattering mechanisms: persistent scatterers (PS) and distributed scatterers (DS). A resolution cell containing a strong scatterer that dominates other scatterer elements inside the pixel is called a persistent scatterer pixel. For example, the phase of a building inside a resolution cell will remain stable through time and appears as a strong scatterer in a sequence of SAR images. Such scattering is the dominant scattering mechanism in urban areas (Osmanoğlu et al. 2011). On the other hand, a distributed scatterer refers to the case where some scatterers are distributed homogenously in a resolution cell. In non-urban areas and natural terrains without dense vegetation, most of the coherent pixels are DS rather than PS (Ferretti et al. 2011).

Depending on the type of coherent pixels, two broad categories of InSAR time-series analysis have been developed. The first one, called persistent scatterer interferometry (PSI), produces a stack of single-master interferograms by selecting one image as the supermaster and the rest of the images as slaves. Then, PS pixels are detected in the stack of single-master interferograms based on the behavior of amplitude or phase of the pixels in space and time (Ferretti et al. 2001, Hooper et al. 2004). In the second category, called Small Baseline Subset (SBAS), a network of multiple-master interferograms with short temporal and spatial baselines is produced. Then, DS pixels are selected based on interferometric coherence (Berardino et al. 2002) or phase statistics of the pixels (Hooper 2008). In recent years, several other approaches have also been proposed for effectively combining PSI and SBAS methods (Ferretti et al. 2011) and increasing the number of detected scatterers for accurate deformation mapping (Bateson et al. 2015, Esmaeili and Motagh 2016).

In this study, we use the PSI and SBAS methods implemented in StaMPS (Stanford Method for Persistent Scatterers) (Hooper 2008, Hooper et al. 2004) for time-series analysis of S-1 data. Having produced a stack of single-master interferograms for PSI or multiple-master interferograms for SBAS, an initial set of coherent pixels is first selected in StaMPS based on the amplitude dispersion of the pixels. In the next step, by statistical analysis of the phase behavior, pixels with high signal to noise ratio are detected, for which the interferometric phase is unwrapped in both spatial and temporal dimensions. Finally, unwanted phase contributions are estimated and eliminated from the time-series of displacement.

3 Large-scale Sentinel-1 processing

S-1 data in IW mode are provided by ESA as 250 km by 250 km Single Look Complex (SLC) images. While the sensor is capable of acquiring data up to 25 minutes in a specific orbit, corresponding to thousands of kilometers, S-1 products are segmented for the aim of simplicity into 250 km slices along a track. However, it is possible to concatenate consecutive frames of data and produce large-scale SLC images along the acquisition track.

ESA provides orbital data for S-1 with three different accuracies; the orbital data attached to the SLC products, the restituted orbit (accuracy of ~10 cm in along and across track directions) which is available a few hours after data acquisition, and precise orbit data (3-D accuracy of ~5 cm) which is available in about 20 days after the acquisition (Yagüe-Martínez et al. 2016). The orbital data attached to the SLC product is usually accurate enough when processing a subset or a full frame of Sentinel-1 data. However, when several frames along the same orbit are joined to form a large-scale SLC image, the precise orbit is needed to improve the accuracy of coregistration, removing the contribution from the orbital phase, and geocoding.

After merging consecutive frames of S-1 to produce a large-SLC image and applying the precise orbital data, it is possible to generate large-scale interferograms as described in the previous section. An example of such an interferogram across Germany is shown in Fig. 3a. This 900-km-long interferogram, formed by joining four

consecutive frames along orbit No. 44, covers a 250-km-wide band across the whole country in a 12-day time span between 7 and 19 January 2016. The orbital and topographic phases are removed by precise orbit data and SRTM 90-meter DEM (Farr and Kobrick 2000).

Aside from some areas where the interferometric phase is decorrelated mainly because of dense vegetation, the quality of the interferometric phase shown in Fig. 3a is high. The interferogram is mostly dominated by fringes in the order of one or more phase cycles over a distance of a few hundred kilometers, which based on Eq. 4 are equivalent to a few centimeters if they are caused by surface deformation (Fig. 3b). Since we do not expect such a long-wavelength displacement in the order of centimeters in Germany, we attribute most of the signal to tropospheric phase delay. To examine this hypothesis, the interferometric phase is compared with the atmospheric phase delays derived from the ERA-Interim global meteorological model and GNSS.

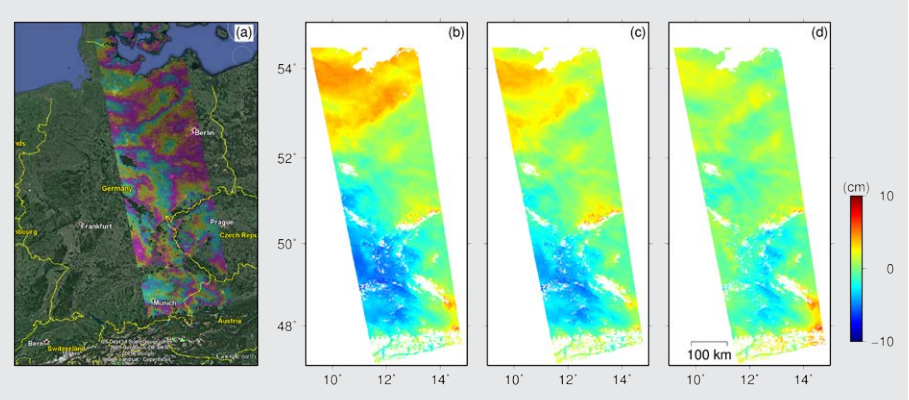

Fig. 3: (a) 900-km long Sentinel-1 interferogram between 7 and 19 January 2016 across Germany. Areas with coherence lower than 0.2 are masked. The background image (a) is from GoogleEarth™, (b) unwrapped phase of the interferogram, (c) and (d) unwrapped phase corrected for atmosphere with ERA-Interim and GNSS models.

The ERA-Interim is a global atmospheric model calculated by European Center for Medium-Range Weather Forecast (ECMWF) based on the assimilation of different input datasets. It provides several meteorological parameters, including pressure, temperature, and relative humidity at 6-hourly intervals at a grid of 70 km spatial resolution and 37 vertical intervals from sea level up to 50 km (Dee et al. 2011). Atmospheric parameters provided by ERA-Interim are interpolated using a vertical and horizontal spline interpolation and a linear interpolation in time to find the atmospheric phase delay from differences in water vapor (wet delay) and atmospheric pressure (hydrostatic delay) at each pixel of the interferogram. The estimated phase delay can then be used to correct the interferogram (Bekaert et al. 2015).

Although positioning is the main aim of GNSS networks, because of redundancy of the recorded data, it is possible to estimate other parameters like the tropospheric phase delay from such networks. With around 350 GNSS stations in Germany, wet delay maps with a spatial resolution of 40 km and in 15 minutes temporal intervals can be estimated (Li et al. 2014). Tropospheric wet delay data derived from GNSS are successfully used to correct InSAR displacement maps (Li et al. 2005, Houlié et al. 2016).

We applied two atmospheric phase delay corrections estimated separately from ERA-Interim data and GNSS products to the S-1 unwrapped interferogram illustrated in Fig. 3b. The results in Fig. 3c-d show that the tropospheric correction based on GNSS data led to a better correction than ERA-Interim. Most of the variations from –10 cm to 10 cm in the unwrapped phase were removed after atmospheric correction using GNSS water vapor maps. ERA-Interim enhanced the RMS (Root Mean Square) of the interferometric phase from 2.7 cm in the original unwrapped interferogram to 2.1 cm in the corrected interferogram (21 % reduction). On the other hand, GNSS-based correction significantly decreased the RMS of the interferometric phase to 1.3 cm in the corrected interferogram (52 % reduction). This is mainly because of the dense network of GNSS permanent stations in Germany and the high temporal resolution of atmospheric products they provide.

It is worth noting that after the tropospheric correction, there are still some residuals left in the interferograms, which can be mainly attributed to turbulent troposphere. This is due to the spatial resolution of the atmospheric models by ERA-Interim or GNSS, which are coarser than the resolution of the S-1 interferograms. Therefore, they are not able to completely remove the turbulent tropospheric effect from the interferograms (Jolivet et al. 2011).

Another interesting point that can be inferred from our analysis in Fig. 3, is the contribution that S-1 interferograms could have in estimating atmospheric parameters in the country scale. In recent years, a few studies have suggested methodologies to use SAR interferometry for atmospheric studies and assimilation into weather models (Alshawaf et al. 2015, Pichelli et al. 2015, Mateus et al. 2016). For atmospheric studies, high spatial resolution is the main power of InSAR, while low temporal resolution and small coverage area, compared to other meteorological inputs, have been described as the major disadvantages of previous SAR missions. In a recent study, Mateus et al. (2017) used S-1 images over the Iberian Peninsula to derive perceptible water vapor maps and suggested the results might be of interest for meteorologists to assimilate them into numerical weather models. Although its temporal resolution is not as high as atmospheric models, with its large coverage and moderate spatial resolution, S-1 InSAR can be assimilated to improve the spatial density of atmospheric models.

4 Anthropogenic Ground Motion in Berlin

In this section, the performance of S-1 InSAR time-series analysis for evaluating localized displacements in an urban area is presented. The study is done in an area of around 10×10 km^2, northwest of Berlin. Since 1992, salt pillows in this area are used as natural underground gas storage for the city of Berlin. The storage is located north of Grunewald forest in densely populated districts of Spandau and Charlottenburg, which makes the monitoring of the reservoir important. Kampes (2005) and Kuehn et al. (2009) used ERS-1/2 data and reported an uplift with a maximum amount of ~5 mm/yr between 1992 and 2005 in the region. In this study, two frames of ascending and two frames of descending S-1 data (listed in Tab. 1) are processed over the study area to investigate the dynamics of the reservoir in the past two years. The area of expected displacement is relatively small in comparison to the overall S-1 scene size. Therefore, only a small subset of each SAR frame that covers the study area is processed. As the study area is mainly urbanized, PSI was used to perform the S-1 InSAR time-series analysis.

Since the study area is small and almost flat, the long-wavelength atmospheric phase delay appears in the S-1 interferograms like a randomly directed ramp. Therefore, a simple linear ramp from each unwrapped interferogram is removed before calculating the average velocity and time-series of displacement. Because of different heading and incidence angles of the data listed in Tab. 1, interferograms produced from each dataset have different sensitivities to horizontal and vertical surface displacement. Assuming the expected displacement is mainly in vertical direction, we neglect the contribution of horizontal displacement and transform the displacement from LOS to the vertical by $v = LOS/\cos\theta$. The vertical displacement rates derived from different datasets are shown in Fig. 4.

Tab. 1: Sentinel-1 SAR dataset used to investigate displacements in Berlin. A/D indicates the orbit (Ascending or Descending) and # shows the number of SAR images. α and θ represent the heading, and incidence angle of the dataset in the study area.

No.	Orbit	A/D	#	Time span	α(°)	θ(°)
1	44	A	61	2014.11.13 – 2017.01.01	351	44
2	95	D	64	2014.10.24 – 2017.01.05	189	43
3	146	A	68	2014.10.27 – 2017.01.02	349	36
4	168	D	63	2014.11.10 – 2017.01.16	191	34

As seen in Fig. 4, most of the urban area is densely covered by PS pixels mainly because buildings act like artificial targets with persistent phase characteristics through time. In the areas with dense vegetation, however, the density of detected pixels is very low. Particularly no persistent pixels are detected in the forested region of Grunewald, except for a line of pixels along the highway in the middle of the forest and a few isolated pixels at the places where some buildings are located.

The results from different datasets show an area of uplift that reaches 2 mm/yr at its peak. Comparing to the older results from ERS-1/2 (Kampes 2005, Kuehn et al. 2009), we can infer that the rate of subsidence has decreased in recent years.

To better investigate the uplift signal, two 200-meter-wide profiles across the uplift area are extracted from the average rate maps (Fig. 5). The first profile follows a 12-km line across the displacement area from northwest to southeast. The second profile is 5 km long from northeast to southwest. A moving average filter with a radius of 200 m was applied on the profiles to increase the signal to noise ratio. Profiles derived from different datasets are in general agreement. The peak of displacement

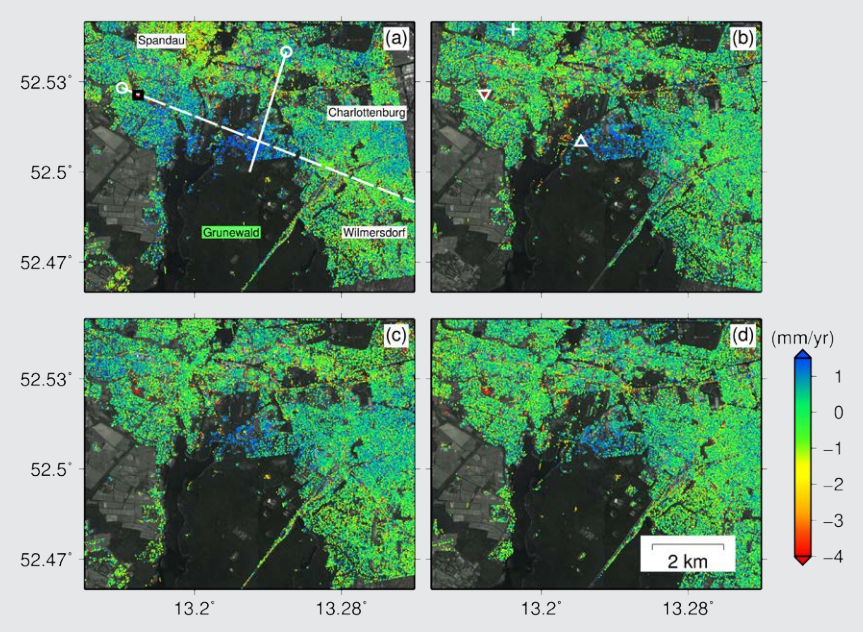

Fig. 4:
(a)–(d) vertical displacement rates obtained by PSI method from Sentinel-1 orbits No. 44, 95, 146 and 168, respectively. The white dashed and thick lines represent the locations of profiles shown in Fig. 5. White circles show the starting point of the profiles. The black square shows the location of a localized subsidence area shown in Fig. 6. Triangles and plus sign show the locations of time-series plotted in Fig. 7. Background image is from GoogleEarth™.

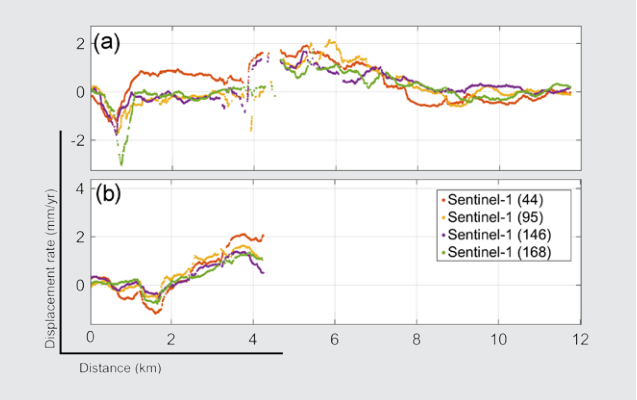

Fig. 5: (a) and (b) Profiles of average velocities along the white dashed and solid lines in Fig. 4 derived from different Sentinel-1 datasets.

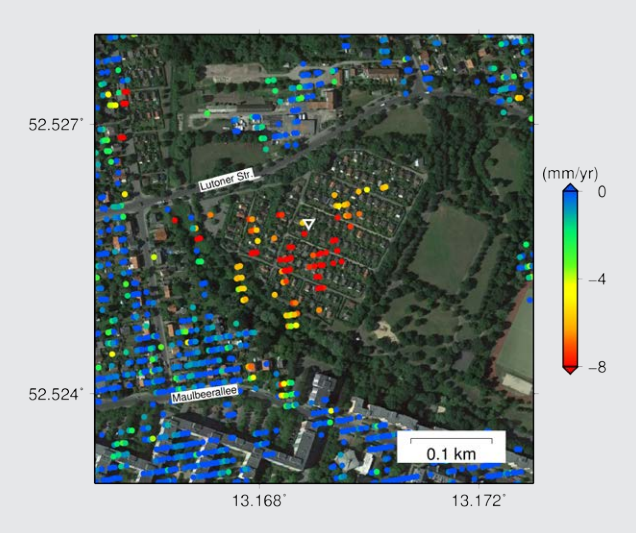

Fig. 6: Vertical displacement rates obtained by PSI method from Sentinel-1 orbit No. 44 in the Egelpfuhl area, west of Berlin. The triangle shows the location of the downward-pointing triangle in Fig. 4b. Background image is from GoogleEarth™.

is located at ~4 to 6 km of the NW-SE profile and ~4 km of the NE-SW profile showing about 2 mm/yr of uplift.

Our results also indicate a subsidence of ~2 mm/yr at approximately 1 km in the NW-SE profile. To better illustrate this, a zoom in the area of subsidence from results obtained using S-1 orbit No. 44 is shown in Fig. 6. The subsidence signal with maximum velocity of 8 mm/yr is related to a small area of about 250 × 250 m^2, called Egelpfuhl; similar results are obtained in this region using other datasets (results not shown here). This area in Berlin was used as a landfill for demolishing waste as well as household waste after the Second World War. In the 2000s, the gas produced from demolishing waste in this landfill was extracted for safety reasons and some gardens where constructed in the area. As seen in Fig. 6, the subsidence is localized in the former landfill area. Therefore, we assume it is most probably related to the settlement of the old demolishing landfill.

Some examples of displacement time-series at different locations (see Fig. 4) are shown in Fig. 7. The time-series (a, d, g, j) show the trend of the displacement in the uplift area. Interestingly, with its dense temporal resolution, S-1 InSAR analysis reflects up to 2 cm of seasonal variations in displacement. The variations are likely to be related to charge and discharge of the storage; we observe uplift during summer time (the period of gas injection) and subsidence during winter time (the extraction period).

The time-series of displacement in the Egelpfuhl landfill area (b, e, h, k) show a clear trend of subsidence with less seasonal fluctuations. To assess the accuracy, the time-series of displacement for a stable point is also plotted (c, f, i, l). This point does not show any clear trend or meaningful variations, confirming that the trend and seasonal variation signals we observed in the displacement areas are not caused by spatially correlated artifacts. The low RMS of the time-series for this stable point (2.5, 1.3, 2.2, and 1.4 mm corresponding to orbit No. 44, 95, 146, and 168, respectively) indicates that the noise level in the

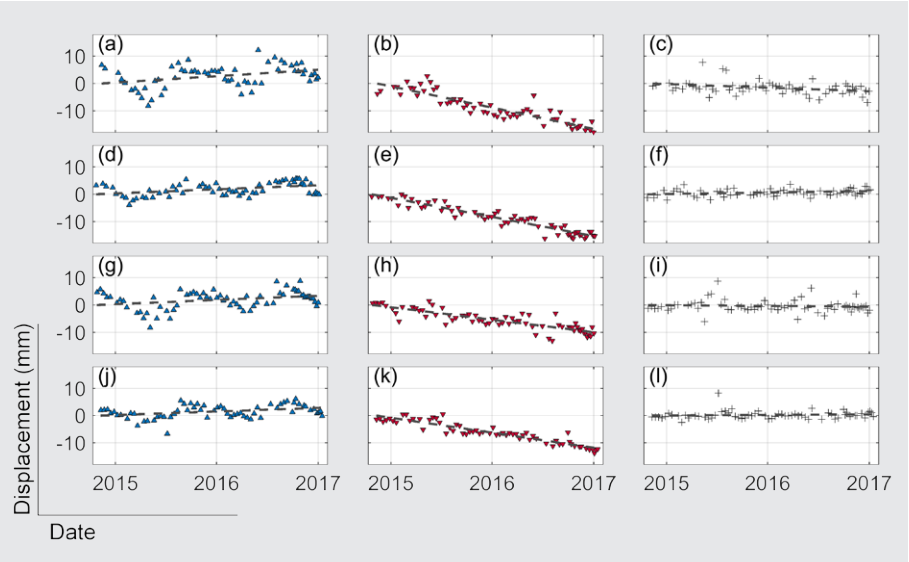

Fig. 7: The time-series of vertical displacements at three different locations for different orbits of the Sentinel-1 dataset: (a-c), (d-f), (g-i), and (j-l) show the results from S-1 orbits No. 44, 95, 146, and 168, respectively. Left, middle, and right panels correspond to the uplift area, the subsidence area, and a stable area away from deformation zones that are shown in Fig. 4 with an upward-pointing triangle, downward-pointing triangle, and plus sign, respectively.

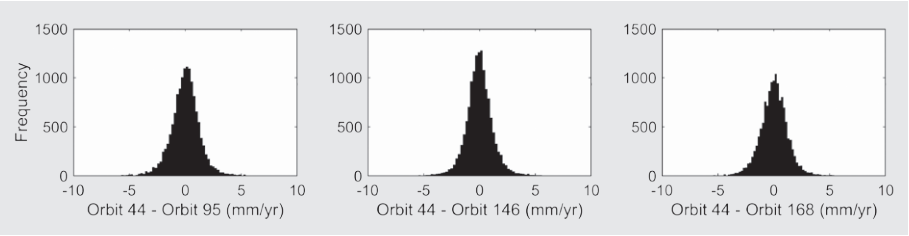

Fig. 8:
Histogram of differences between average velocities in Berlin estimated from Sentinel-1 orbits No. 95, 146, and 168 with respect to orbit No. 44.

time-series of the displacements is in the order of a few millimeters (< 2.5 mm).

To evaluate the consistency of the results derived from different S-1 datasets (Fig. 4), the discrepancy between them is estimated and the RMS of the differences is used as a measure of accuracy. Histograms of differences between average velocities estimated from orbits No. 95, 146, and 168 with respect to orbit No. 44 are illustrated in Fig. 8. Small differences (RMS equal to 1.4, 1.3, and 1.3 mm/yr for orbit No. 95, 146, and 168) confirm that the results from different datasets are in good agreement.

5 Mining-induced deformation in Leipzig

Our second case study addresses an area subject to rapid displacement caused by open-pit mining activities near the city of Leipzig. A total area of 200 km^2 south of Leipzig has been a major reservoir providing brown coal for more than a century. Intense mining activities have dramatically changed the landscape, the geological and the hydrological situation of the region (Birkhölzer et al. 1998). During the mining activities, the groundwater level was lowered to below the mining level to make open-pit mining possible. After the reunification of Germany, several open-pit mines in the region were abandoned. Followed by rising of groundwater, some were filled with water and became lakes. There are still two major active mines in the region, which provide coal for power plants in the area. They were opened in the 1940s and expected to be running until the 2030s. In total they produce 20 million tons of brown coal each year. Land subsidence is an expected phenomenon in the mining areas south of Leipzig as a result of groundwater withdrawal (Wolkersdorfer and Thiem 1999). Schäfer et al. (2007) used ERS2 and Envisat data in this region and reported displacements in the order of ±1 cm over two years.

Tab. 2: Sentinel-1 SAR dataset used to investigate displacements in the mining area south of Leipzig. A/D indicates the orbit (Ascending or Descending) and # shows the number of images. α and θ represent the heading and incidence angle of the SAR dataset, respectively.

No.	Orbit	A/D	#	Time span	α(°)	θ(°)
1	44	A	81	2014.10.20 – 2017.04.07	350	40
2	168	D	75	2014.10.17 – 2017.04.10	190	37

We used a collection of S-1 images between 2014.10.17 and 2017.04.10 in ascending and descending tracks to investigate the displacements in this area (see Tab. 2 for details). Because the area is not urbanized and most of coherent pixels are expected to be DS, the SBAS approach was used and a network of small baseline interferograms was produced for each track of data. In total, 205 and 270 small baseline interferograms were generated corresponding to Sentinel-1 orbit No. 44 and 168 respectively. The network was inverted using the least-squares approach and the average rate and time-series of displacement were estimated.

The 12-meter TanDEM-X DEM was used in the processing to remove the topographic phase from the interferograms. The resolution and accuracy of the TanDEM-X DEM used in the processing are high, but because the DEM was produced a few years before Sentinel-1

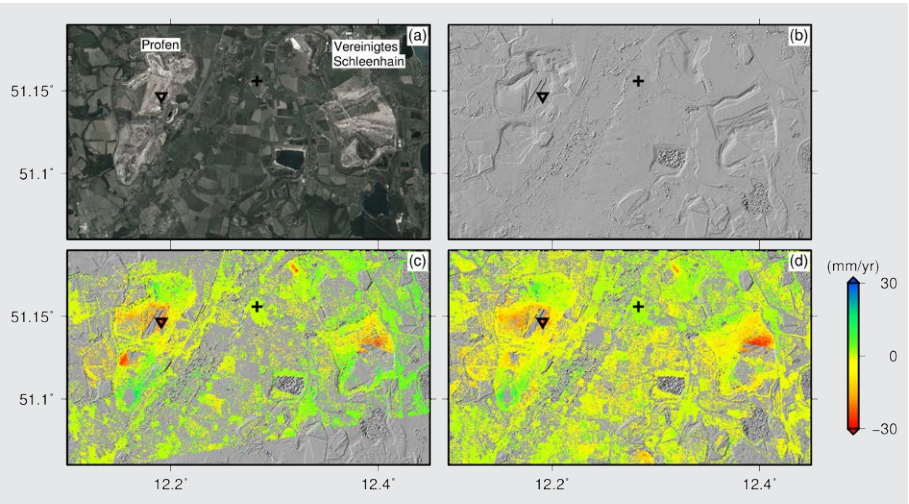

Fig. 9:
(a) GoogleEarth™ view of the active mining area south of Leipzig, (b) shaded relief map of the study area derived from TanDEM-X 12-meter DEM, (c) and (d) average velocity maps in the LOS direction from the satellite to the ground, derived from the SBAS analysis of Sentinel-1 orbits No. 44 and 168, respectively. Downward-pointing triangles and plus signs show the location of the time-series plots in Fig. 10.

acquisitions, any changes in topography, which is not unexpected in active mining areas, can cause unwanted phase residual in the interferograms. Based on Eq. 2, for a Sentinel-1 interferogram in our study area with a perpendicular baseline of 85 m and an incidence angle of 40°, an error of ~200 m in the DEM causes a complete phase cycle, which can be misinterpreted as 2.6 cm of displacement. To restrain the topographic residuals only interferograms with short perpendicular baselines (maximum 85 m) were used in the SBAS network. Furthermore, after interferograms are unwrapped, spatially-correlated DEM errors, that are proportional to perpendicular baselines, are estimated and removed from the unwrapped interferograms.

Fig. 9a-b show the GoogleEarth™ image of the study area and its shaded relief map, respectively. Two active open-pit mining areas are indicated in this figure. Some older mines that were filled with water and became lakes are also visible in the eastern part of this figure. Fig. 9c-d show the average LOS velocities from the S-1 time-series analysis. Although the vegetation cover in some areas caused low density of detected pixels, the density in the mining areas is high except for some regions that are most probably subject to rapid changes and thus loss of coherence due to mining activities. While the areas away from active mines do not show any significant displacement, the two active mining areas and their surroundings show some strong displacement signals.

The displacement rates in the mining area reach a maximum amount of 30 mm/yr away from the satellite at some locations. The time-series of displacement in the main deforming region is mostly dominated by a linear declining trend in time, as illustrated in Fig. 10. Time-series of displacement in a non-deforming area does not show much variation (RMS equal to 2.7 mm and 1.7 mm for orbits No. 44 and 168, respectively), which confirms that the magnitude of unwanted signals in the time-series is low in comparison to cm-scale displacement signal that we observe in the mining area.

To estimate the consistency between the two datasets, the average velocities in Fig. 9 are first transformed from LOS to vertical direction by neglecting the horizontal displacement, and then are compared with each other. Fig. 11 illustrates the histogram of differences between the average vertical velocities. The RMS of differences between ascending and descending results is approximately 6 mm/yr that verifies their consistency. However, this RMS of the differences between datasets in Leipzig is higher than those in Berlin. We attribute this to neglecting the contribution of horizontal displacements. For example, based on Eq. 5 and imaging geometries of the S-1 dataset in Tab. 2, 10 mm/yr of displacement in East-West direction will project on the line-of-sight as movements equal to 6 mm/yr towards the satellite for descending orbits and 6 mm/yr away from the satellite for ascending orbits in our study area. When horizontal movements are neglected, such a displacement can be misinterpreted as 7 mm/yr of subsidence and 8 mm/yr of uplift in descending and ascending orbits, respectively. As a result, the RMS of differences between average velocities of different datasets might increase by neglected horizontal displacements.

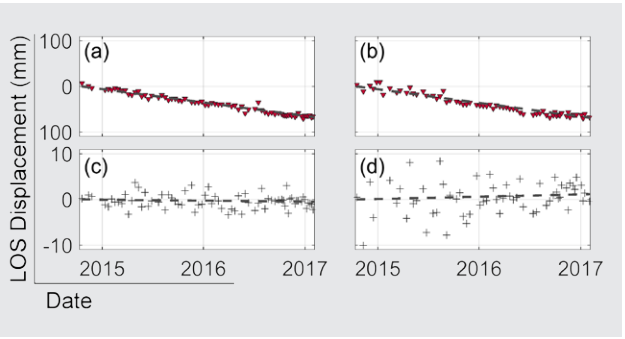

Fig. 10: Examples of LOS displacement time-series at: (a, b) a subsidence area (downward-pointing triangle in Fig. 9) in the active mining region, and (c, d) a non-deforming area (plus sign in Fig. 9). (a, c) and (b, d) correspond to results derived from S-1 orbits No. 44 and 168.

We take advantage of different imaging geometries of datasets to estimate the vertical and horizontal components of displacement. Based on Eq. 5, the sensitivity of line-of-sight measurements in our study area to the south-north motions is only 11 %, while it is about 60 % and 80 % for east-west and vertical motions. Therefore, we neglect the south-north component of motion and estimate east-west and vertical displacement rates from the two line-of-sight velocities. The results are shown in Fig. 12. As seen in Fig. 12, the maximum amount

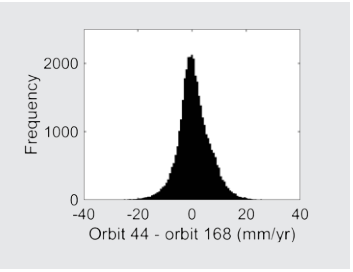

Fig. 11: Histogram of differences for vertical displacement rates in Leipzig derived from different Sentinel-1 datasets.

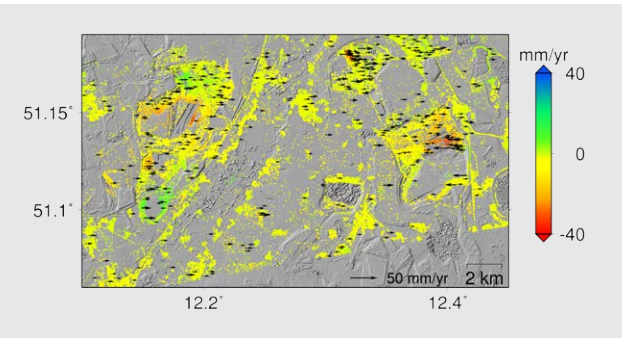

Fig. 12: Vertical and east-west displacement rates in active mining area south of Leipzig. The background colors are vertical displacement rates and arrows are horizontal motions. For a better visualization, only 90 % of vectors with east-west displacement larger than 1 cm/yr are shown in this figure.

of vertical displacement rates reaches 40 mm/yr around active mining areas. As expected, horizontal motion increases in regions with high gradients of vertical movement and reaches maximum rates of 48 mm/yr at some locations.

6 Conclusions and prospect

In this paper, some highlights of Sentinel-1 SAR interferometry in Germany were presented to evaluate the potential and possibilities provided by this technique for deformation monitoring and atmospheric phase delay analysis. First, a 900-km-long Sentinel-1 interferogram across the country was presented. Atmospheric corrections revealed that most of ±10 cm phase change in this interferogram was caused by tropospheric wet delay. The atmospheric water vapor estimated from a dense network of GNSS measurements improved the quality of the interferogram by 52 % while ERA-Interim could improve it by 21 %. Although tropospheric phase delay is a disadvantage for displacement applications, with its large spatial coverage and high spatial density, Sentinel-1 provides great opportunities for atmospheric studies. Future research should focus on incorporating/assimilating InSAR measurements in atmospheric models. In particular, the major phase contribution in Sentinel-1 interferograms with short time intervals in mid-latitudes comes from changes in water vapor at the time of image pair acquisitions. Therefore, it can produce an estimate of relative water vapor conditions at the times of acquisitions that can be of interest for meteorologists.

Secondly, we demonstrated the capability of S-1 time-series analysis for monitoring small-magnitude displacements related to gas storage and landfill compaction in north-western part of Berlin and cm-scale displacements due to active mining in Leipzig. With its 6-day acquisition time interval, large coverage, and moderate spatial resolution, Sentinel-1 provides new emerging opportunities to investigate localized displacements in much more temporal details than currently possible with other satellite-based SAR systems. We have observed a maximum of ~2 mm/yr uplift during October 2014 to January 2017, and up to 2 cm of variations due to seasonal charge and discharge of the gas storage. A localized subsidence signal of ~8 mm/yr, due to the settlement of the old demolishing landfill and gas extraction in Egelpfuhl, northwest of Berlin, was also detected. For the mining area in Leipzig, subsidence rates as much as 4 cm/yr in active mining areas were found for the period between October 2014 and April 2017.

Although we did not have access to ground truth for validation and accuracy assessment of our InSAR time-series results, statistical analyses of the results enabled us to evaluate their consistency with each other and provided a measure of accuracy that we can achieve by S-1 InSAR time-series analyses. The RMS of differences between average velocities derived from different Sentinel-1 datasets was <1.4 mm/yr and 6 mm/yr for Berlin and Leipzig, respectively. The maximum RMS of the time-series of displacements at stable areas was approx. 3 mm that shows the power of Sentinel-1 InSAR time-series analyses to detect displacements with magnitudes of as small as a few millimeters.

With its free data policy and 20-year acquisition plan, Sentinel-1 provides great opportunities for InSAR geodesy to be widely applied by both scientific and commercial users to generate information for the purpose of hazard and risk management related to natural and man-made phenomena. In the future, developing new methodologies to automatically obtain the data, detecting areas prone to a specific process, and obtaining the results from appropriate InSAR time-series approaches can help us extract the maximum benefit from near real-time SAR data provided by Sentinel-1. At the same time, new challenges arise for handling of the massive datasets provided by the mission. Sentinel-1 provides 10 TB of products daily. With its large spatial coverage and medium resolution, each SLC data of this sensor is in the order of a few GB. Mosaicking these images along a specific orbit and interferometric processing multiply the need for disk space and dramatically increases the required processing loud that can be challenging to handle. Development of innovative processing chains using cloud-based systems like ESA's Geohazards Exploitation Platform GEP (De Luca et al. 2015) or CODE-DE (Copernicus Data and Exploitation Platform – Deutschland) (Reck et al. 2016) should be further explored in future to deal with the huge amounts of SAR data provided by the Sentinel-1 constellation.

Acknowledgements

We thank Fadwa Alshawaf and Galina Dick from GFZ for providing water vapor models from GNSS observations. We thank Dr. Wetzel from GFZ for translating the abstract in German. This work was supported by Initiative and Networking Fund of the Helmholtz Association in the frame of Helmholtz Alliance "Remote Sensing and Earth System Dynamics". TanDEM-X DEM data are provided by DLR under proposal number motagh_IDEM_GEOL0157. Some figures were generated using Generic Mapping Tools (Wessel et al. 2013). Sentinel-1 data were provided by ESA.

References

Adam, N., Gonzalez, F.R., Parizzi, A., Brcic, R.: Wide area Persistent Scatterer Interferometry: Current developments, algorithms and examples. IEEE International Geoscience and Remote Sensing Symposium (IGARSS), pp. 1857–1860, 2013.

Alshawaf, F., Fersch, B., Hinz, S., Kunstmann, H., Mayer, M., Thiele, A., Westerhaus, M., Meyer, F.: Analysis of atmospheric signals in spaceborne InSAR – toward water vapor mapping based on multiple sources. Geoscience and Remote Sensing Symposium (IGARSS), pp. 1960–1963, 2012.

Alshawaf, F., Hinz, S., Mayer, M., Meyer, F.J.: Constructing accurate maps of atmospheric water vapor by combining interferometric synthetic aperture radar and GNSS observations. J. Geophys. Res.: Atmos. 120, pp. 1391–1403, 2015.

Bateson, L., Cigna, F., Boon, D., Sowter, A.: The application of the Intermittent SBAS (ISBAS) InSAR method to the South Wales Coalfield, UK. Int. J. Appl. Earth Obs. Geoinf. 34, pp. 249–257, 2015.

Bekaert, D.P.S., Walters, R.J., Wright, T.J., Hooper, A.J., Parker, D.J.: Statistical comparison of InSAR tropospheric correction techniques. Remote Sens. Environ. 170, pp. 40–47, 2015.

Berardino, P., Fornaro, G., Lanari, R., Sansosti, E.: A new algorithm for surface deformation monitoring based on small baseline differential SAR interferograms. IEEE Trans. Geosci. Remote Sens. 40, pp. 2375–2383, 2002.

Birkhölzer, J., Opheys, S., Rouvé, G.: A Conceptual Study on the Rehabilitation of the Lignite Mining Area South of Leipzig. In: D.P. Loucks (Ed.), Restoration of Degraded Rivers: Challenges, Issues and Experiences. Dordrecht: Springer Netherlands, pp. 99–110, 1998.

Bürgmann, R., Rosen, P.A., Fielding, E.J.: Synthetic Aperture Radar Interferometry to Measure Earth's Surface Topography and Its Deformation. Annu. Rev. Earth Planet. Sci. 28, pp. 169–209, 2000.

Castel, T., Martinez, J.-M., Beaudoin, A., Wegmüller, U., Strozzi, T.: ERS INSAR Data for Remote Sensing Hilly Forested Areas. Remote Sens. Environ. 73, pp. 73–86, 2000.

De Luca, C., Cuccu, R., Elefante, S., Zinno, I., Manunta, M., Casola, V., Rivolta, G., Lanari, R., Casu, F.: An On-Demand Web Tool for the Unsupervised Retrieval of Earth, Äôs Surface Deformation from SAR Data: The P-SBAS Service within the ESA G-POD Environment. Remote Sens. 7, pp. 15630–15650, 2015.

Dee, D.P., Uppala, S.M., Simmons, A.J., Berrisford, P., Poli, P., Kobayashi, S., Andrae, U., Balmaseda, M.A., Balsamo, G., Bauer, P., Bechtold, P., Beljaars, A.C.M., van de Berg, L., Bidlot, J., Bormann, N., Delsol, C., Dragani, R., Fuentes, M., Geer, A.J., Haimberger, L., Healy, S.B., Hersbach, H., Hólm, E.V., Isaksen, L., Kållberg, P., Köhler, M., Matricardi, M., McNally, A.P., Monge-Sanz, B.M., Morcrette, J.J., Park, B.K., Peubey, C., de Rosnay, P., Tavolato, C., Thépaut, J.N., Vitart, F.: The ERA-Interim reanalysis: configuration and performance of the data assimilation system. Q.J.R. Meteorolog. Soc. 137, pp. 553–597, 2011.

Emadali, L., Motagh, M., Haghshenas Haghighi, M.: Characterizing post-construction settlement of the Masjed-Soleyman embankment dam, Southwest Iran, using TerraSAR-X SpotLight radar imagery. Eng. Struct. 143, pp. 261–273, 2017.

Esmaeili, M., Motagh, M.: Improved Persistent Scatterer analysis using Amplitude Dispersion Index optimization of dual polarimetry data. ISPRS J. Photogramm. Remote Sens. 117, pp. 108–114, 2016.

Farr, T.G., Kobrick, M.: Shuttle radar topography mission produces a wealth of data. EOS Trans., Am. Geophys. Union 81, pp. 583–585, 2000.

Ferretti, A., Fumagalli, A., Novali, F., Prati, C., Rocca, F., Rucci, A.: A New Algorithm for Processing Interferometric Data-Stacks: SqueeSAR. IEEE Trans. Geosci. Remote Sens. 49, pp. 3460–3470, 2011.

Ferretti, A., Prati, C., Rocca, F.: Permanent scatterers in SAR interferometry. IEEE Trans. Geosci. Remote Sens. 39, pp. 8–20, 2001.

Fornaro, G., Reale, D., Verde, S.: Bridge Thermal Dilation Monitoring With Millimeter Sensitivity via Multidimensional SAR Imaging. IEEE Geosci. Remote Sens. Lett. 10, pp. 677–681, 2013.

Francesca, C., Luke, B., Colm, J., Claire, D.: Nationwide monitoring of geohazards in Great Britain with InSAR: Feasibility mapping based on ERS-1/2 and ENVISAT imagery. In: IEEE International Geoscience and Remote Sensing Symposium – (IGARSS). pp. 672–675, 2013.

Fuhrmann, T., Knöpfler, A., Mayer, M., Schenk, A., Westerhaus, M., Zippelt, K., Heck, B.: An Inventory of Surface Movements in the Upper Rhine Graben Area, Southwest Germany, from SAR-Interferometry, GNSS and Precise Levelling. In: Rizos, C., Willis, P. (eds): IAG 150 Years. International Association of Geodesy Symposia, Springer, Cham, pp. 419–425, 2016.

González, P.J., Bagnardi, M., Hooper, A.J., Larsen, Y., Marinkovic, P., Samsonov, S.V., Wright, T.J.: The 2014–2015 eruption of Fogo volcano: Geodetic modeling of Sentinel-1 TOPS interferometry. Geophys. Res. Lett. 42, pp. 9239–9246, 2015.

Gourmelen, N., Amelung, F., Lanari, R.: Interferometric synthetic aperture radar-GPS integration: Interseismic strain accumulation across the Hunter Mountain fault in the eastern California shear zone. J. Geophys. Res.: Solid Earth, 115, 2010.

Haghshenas Haghighi, M., Motagh, M.: Assessment of ground surface displacement in Taihape landslide, New Zealand, with C- and X-band SAR interferometry. N.Z.J. Geol. Geophys., 59, pp. 136–146, 2016.

Hanssen, Ramon F.: Rhadar interferometry: data interpretation and error analysis. Kluwer Academic Publishers, The Netherlands, 2001.

Heimlich, C., Gourmelen, N., Masson, F., Schmittbuhl, J., Kim, S.-W., Azzola, J.: Uplift around the geothermal power plant of Landau (Germany) as observed by InSAR monitoring. Geotherm. Energy 3, 2015.

Hole, J.K., Bromley, C.J., Stevens, N.F., Wadge, G.: Subsidence in the geothermal fields of the Taupo Volcanic Zone, New Zealand from 1996 to 2005 measured by InSAR. J. Volcanol. Geotherm. Res. 166, pp. 125–146, 2007.

Hooper, A., Bekaert, D., Spaans, K., Arıkan, M.: Recent advances in SAR interferometry time series analysis for measuring crustal deformation. Tectonophysics 514–517, pp. 1–13, 2012.

Hooper, A., Segall, P., Zebker, H. Persistent scatterer interferometric synthetic aperture radar for crustal deformation analysis, with application to Volcán Alcedo, Galápagos. J. Geophys. Res. B: Solid Earth 112, 2007.

Hooper, A., Zebker, H., Segall, P., Kampes, B.: A new method for measuring deformation on volcanoes and other natural terrains using InSAR persistent scatterers. Geophys. Res. Lett. 31, 2004.

Hooper, A.: A multi-temporal InSAR method incorporating both persistent scatterer and small baseline approaches. Geophys. Res. Lett. 35, 2008.

Houlié, N., Funning, G.J., Bürgmann, R.: Use of a GPS-Derived Troposphere Model to Improve InSAR Deformation Estimates in the San Gabriel Valley, California. IEEE Trans. Geosci. Remote Sens. 54, pp. 5365–5374, 2016.

Jolivet, R., Grandin, R., Lasserre, C., Doin, M.P., Peltzer, G.: Systematic InSAR tropospheric phase delay corrections from global meteorological reanalysis data. Geophys. Res. Lett. 38, 2011.

Kampes, B.M.: Displacement parameter estimation using permanent scatterer interferometry. Doctoral dissertation. TU Delft, Delft University of Technology, The netherlands, 2005.

Kircher, M., Roth, A., Adam, N., Kampes, B., Neugebauer, H.J.: Remote sensing observation of mining induced subsidence by means of differential SAR-interferometry. IEEE International Geoscience and Remote Sensing Symposium – (IGARSS), pp. 209–211, 2003.

Kuehn, F., Hoth, P., Stark, M., Burren, R., Hole, J.: Experience with Satellite Radar for Gas Storage Monitoring. Erdöl Erdgas Kohle, 125, 2009.

Kumar, V., Venkataraman, G., Rao, Y.S., Singh, G., Snehmani: Spaceborne InSAR Technique for Study of Himalayan Glaciers using ENVISAT ASAR and ERS Data. IEEE International Geoscience and Remote Sensing Symposium (IGARSS), 2008.

Li, X., Dick, G., Ge, M., Heise, S., Wickert, J., Bender, M.: Real-time GPS sensing of atmospheric water vapor: Precise point positioning with orbit, clock, and phase delay corrections. Geophys. Res. Lett. 41, pp. 3615–3621, 2014.

Li, Z., Muller, J.Ä., Cross, P., Fielding, E.J.: Interferometric synthetic aperture radar (InSAR) atmospheric correction: GPS, Moderate Resolution Imaging Spectroradiometer (MODIS), and InSAR integration. J. Geophys. Res. B: Solid Earth. 110, 2005.

Liu, D., Sowter, A., Niemeier, W.: Process-related deformation monitoring by PSI using high resolution space-based SAR data: a case study in Düsseldorf, Germany. Nat. Hazards Earth Syst. Sci. Discuss. 2, pp. 4813–4830, 2014.

Lu, Z., Kwoun, O.I.: Radarsat-1 and ERS InSAR Analysis Over Southeastern Coastal Louisiana: Implications for Mapping Water-Level Changes Beneath Swamp Forests. IEEE Trans. Geosci. Remote Sens. 46, pp. 2167–2184, 2008.

Lubitz, C., Motagh, M., Wetzel, H.-U., Kaufmann, H.: Remarkable Urban Uplift in Staufen im Breisgau, Germany: Observations from TerraSAR-X InSAR and Leveling from 2008 to 2011. Remote Sens. 5, pp. 3082–3100, 2013.

Massonnet, D., Feigl, K.L.: Radar interferometry and its application to changes in the Earth's surface. Rev. Geophys. 36, pp. 441–500, 1998.

Mateus, P., Catalão, J., Nico, G.: Sentinel-1 Interferometric SAR Mapping of Precipitable Water Vapor Over a Country-Spanning Area. IEEE Trans. Geosci. Remote Sens. 55, pp. 2993–2999, 2017.

Mateus, P., Tomé, R., Nico, G., Catalão, J.: Three-Dimensional Variational Assimilation of InSAR PWV Using the WRFDA Model. IEEE Trans. Geosci. Remote Sens. 54, pp. 7323–7330, 2016.

Milillo, P., Bürgmann, R., Lundgren, P., Salzer, J., Perissin, D., Fielding, E., Biondi, F., Milillo, G.: Space geodetic monitoring of engineered structures: The ongoing destabilization of the Mosul dam, Iraq. Sci. Rep., 6, 37408, 2016.

Millin-Chalabi, G., McMorrow, J., Agnew, C.: Detecting a moorland wildfire scar in the Peak District, UK, using synthetic aperture radar from ERS-2 and Envisat ASAR. Int. J. Remote Sens, 35, pp. 54–69, 2014.

Motagh, M., Schurr, B., Anderssohn, J., Cailleau, B., Walter, T.R., Wang, R., Villotte, J.-P.: Subduction earthquake deformation associated with 14 November 2007, Mw 7.8 Tocopilla earthquake in Chile: Results from InSAR and aftershocks. Tectonophysics 490, pp. 60–68, 2010.

Motagh, M., Shamshiri, R., Haghshenas Haghighi, M., Wetzel, H.-U., Akbari, B., Nahavandchi, H., Roessner, S., Arabi, S.: Quantifying groundwater exploitation induced subsidence in the Rafsanjan plain, southeastern Iran, using InSAR time-series and in situ measurements. Eng. Geol. 218, pp. 134–151, 2017.

Motagh, M., Walter, T.R., Sharifi, M.A., Fielding, E., Schenk, A., Anderssohn, J., Zschau, J.: Land subsidence in Iran caused by widespread water reservoir overexploitation. Geophys. Res. Lett. 35, 2008a.

Motagh, M., Wang, R., Walter, T.R., Bürgmann, R., Fielding, E., Anderssohn, J., Zschau, J.: Coseismic slip model of the 2007 August Pisco earthquake (Peru) as constrained by wide swath radar observations. Geophys. J. Int. 174, pp. 842–848, 2008b.

Osmanoğlu, B., Dixon, T.H., Wdowinski, S., Cabral-Cano, E., Jiang, Y.: Mexico City subsidence observed with persistent scatterer InSAR. Int. J. Appl. Earth Obs. Geoinf. 13, pp. 1–12, 2011.

Pichelli, E., Ferretti, R., Cimini, D., Panegrossi, G., Perissin, D., Pierdicca, N., Rocca, F., Rommen, B.: InSAR Water Vapor Data Assimilation into Mesoscale Model MM5: Technique and Pilot Study. IEEE J. Sel. Top. Appl. Earth Obs. Remote Sens. 8, pp. 3859–3875, 2015.

Pritchard, M.E., Fielding, E.J.: A study of the 2006 and 2007 earthquake sequence of Pisco, Peru, with InSAR and teleseismic data. Geophys. Res. Lett. 35, 2008.

Raspini, F., Bianchini, S., Del Ventisette, C., Moretti, S., Loupasakis, C., Rozos, D., Duro, J., Garcia, M.: Subsidence mapping, characterization, and modeling: the ESA-GMES Terrafirma services. Third International Conference on Remote Sensing and Geoinformation of the Environment, 2015.

Reck, C., Campuzano, G., Dengler, K., Heinen, T., Winkler, M.: German Copernicus Data Access and Exploitation Platform. Proceedings of 2016 conference on Big Data from Space: Publications Office of the European Union, pp. 1–4, 2016.

Salvi, S., Stramondo, S., Funning, G.J., Ferretti, A., Sarti, F., Mouratidis, A.: The Sentinel-1 mission for the improvement of the scientific understanding and the operational monitoring of the seismic cycle. Remote Sens. Environ. 120, pp. 164–174, 2012.

Samsonov, S., d'Oreye, N., Smets, B.: Ground deformation associated with post-mining activity at the French-German border revealed by novel InSAR time series method. Int. J. Appl. Earth Obs. Geoinf. 23, pp. 142–154, 2013.

Samsonov, S.V., d'Oreye, N., González, P.J., Tiampo, K.F., Ertolahti, L., Clague, J.J.: Rapidly accelerating subsidence in the Greater Vancouver region from two decades of ERS-ENVISAT-RADARSAT-2 DInSAR measurements. Remote Sens. Environ. 143, pp. 180–191, 2014.

Santoro, M., Askne, J.I.H., Wegmuller, U., Werner, C.L.: Observations, Modeling, and Applications of ERS-ENVISAT Coherence Over Land Surfaces. IEEE Trans. Geosci. Remote Sens. 45, pp. 2600–2611, 2007.

Schäfer, M., Walter, D., Busch, W.: DInSAR ground movement monitoring in the rural environment of an open pit mining area. ENVISAT Symposium (ESA SP-636). Montreux, Switzerland, 2007.

Scheiber, R., Moreira, A.: Coregistration of interferometric SAR images using spectral diversity. IEEE Trans. Geosci. Electron., 38, pp. 2179–2191, 2000.

Torres, R., Snoeij, P., Geudtner, D., Bibby, D., Davidson, M., Attema, E., Potin, P., Rommen, B., Floury, N., Brown, M., Traver, I., Deghaye, P., Duesmann, B., Rosich, B., Miranda, N., Bruno, C., L'Abbate, M., Croci, R., Pietropaolo, A., Huchler, M., Rostan, F.: GMES Sentinel-1 mission. Remote Sens. Environ. 120, pp. 9–24, 2012.

Walter, D., Wegmüller, U., Spreckels, V., Hannemann, W., Busch, W.: Interferometric monitoring of an active underground mining field with high-resolution SAR sensors. In: Proceedings of ISPRS Workshop. Hannover, Germany, 2009.

Wegmuller, U., Strozzi, T., Werner, C., Wiesmann, A., Benecke, N., Spreckels, V.: Monitoring of mining-induced surface deformation in the Ruhrgebiet (Germany) with SAR interferometry. Geoscience and Remote Sensing Symposium, pp. 2771–2773, 2000.

Wegmuller, U., Werner, C., Strozzi, T., Wiesmann, A.: Monitoring mining induced surface deformation. Geoscience and Remote Sensing Symposium, vol. 3, pp. 1933–1935, 2004.

Werner, Z., Russ, P., Iris, L., Richard, C., Dieter, H.: The PRESENSE and PIPEMON projects – defining the ways of using space-borne earth observation services for pipeline monitoring. In: Proceedings International Gas Research Conference, Vancouver, Canada. 2004.

Wessel, P., Smith, W.H.F., Scharroo, R., Luis, J.F., Wobbe, F.: Generic Mapping Tools: Improved version released, EOS Trans. AGU, 94, pp. 409–410, 2013.

Wolkersdorfer, C., Thiem, G.: Ground water withdrawal and land subsidence in northeastern Saxony (Germany). Mine Water Environ. 18, pp. 81–92, 1999.

Xiuming, J.I.A., Chao, M.A., Anyuan, Z.: Environmental Investigation and Evaluation of Land Subsidence in the Datong Coalfield Based on InSAR Technology. Acta Geol. Sin. – English Edition 82, pp. 1035–1044, 2008.

Yagüe-Martínez, N., Prats-Iraola, P., González, F.R., Brcic, R., Shau, R., Geudtner, D., Eineder, M., Bamler, R.: Interferometric Processing of Sentinel-1 TOPS Data. IEEE Trans. Geosci. Remote Sens. 54, pp. 2220–2234, 2016.

Zan, F.D., Guarnieri, A.M.M.: TOPSAR: Terrain Observation by Progressive Scans. IEEE Trans. Geosci. Remote Sens. 44, pp. 2352–2360, 2006.

Zebker, H.A., Rosen, P.A., Hensley, S.: Atmospheric effects in interferometric synthetic aperture radar surface deformation and topographic maps. J. Geophys. Res. B: Solid Earth 102, pp. 7547–7563, 1997.

Contact

Mahmud Haghshenas Haghighi | Mahdi Motagh

GFZ German Research Center for Geosciences, Department of Geodesy, Section of Remote Sensing, 14473 Potsdam, Germany

and

Institute of Photogrammetry and GeoInformation, Leibniz Universität Hannover, 30167 Hannover, Germany

mahmud@gfz-potsdam.de | motagh@gfz-potsdam.de

This article also is digitally available under www.geodaesie.info.